BRAIN
ORIGINAL ARTICLE

Cell-type specific and multiscale dynamics of human focal seizures in limbic structures

Alexander H. Agopyan-Miu,[1,†] Edward M. Merricks,[2,†] Elliot H. Smith,[2,3] Guy M. McKhann II,[1] Sameer A. Sheth,[4] Neil A. Feldstein,[1] Andrew J. Trevelyan[5] and Catherine A. Schevon[2]

[†]These authors contributed equally to this work.

The relationship between clinically accessible epileptic biomarkers and neuronal activity underlying the transition to seizure is complex, potentially leading to imprecise delineation of epileptogenic brain areas. In particular, the pattern of interneuronal firing at seizure onset remains under debate, with some studies demonstrating increased firing and others suggesting reductions. Previous study of neocortical sites suggests that seizure recruitment occurs upon failure of inhibition, with intact feedforward inhibition in non-recruited territories. We investigated whether the same principle applies in limbic structures.

We analysed simultaneous electrocorticography (ECoG) and neuronal recordings of 34 seizures in a cohort of 19 patients (10 male, 9 female) undergoing surgical evaluation for pharmacoresistant focal epilepsy. A clustering approach with five quantitative metrics computed from ECoG and multiunit data was used to distinguish three types of site-specific activity patterns during seizures, which at times co-existed within seizures. Overall, 156 single units were isolated, subclassified by cell-type and tracked through the seizure using our previously published methods to account for impacts of increased noise and single-unit waveshape changes caused by seizures.

One cluster was closely associated with clinically defined seizure onset or spread. Entrainment of high-gamma activity to low-frequency ictal rhythms was the only metric that reliably identified this cluster at the level of individual seizures ($P < 0.001$). A second cluster demonstrated multi-unit characteristics resembling those in the first cluster, without concomitant high-gamma entrainment, suggesting feedforward effects from the seizure. The last cluster captured regions apparently unaffected by the ongoing seizure. Across all territories, the majority of both excitatory and inhibitory neurons reduced (69.2%) or ceased firing (21.8%). Transient increases in interneuronal firing rates were rare (13.5%) but showed evidence of intact feedforward inhibition, with maximal firing rate increases and waveshape deformations in territories not fully recruited but showing feedforward activity from the seizure, and a shift to burst-firing in seizure-recruited territories ($P = 0.014$).

This study provides evidence for entrained high-gamma activity as an accurate biomarker of ictal recruitment in limbic structures. However, reduced neuronal firing suggested preserved inhibition in mesial temporal structures despite simultaneous indicators of seizure recruitment, in contrast to the inhibitory collapse scenario documented in neocortex. Further study is needed to determine if this activity is ubiquitous to hippocampal seizures or indicates a 'seizure-responsive' state in which the hippocampus is not the primary driver. If the latter, distinguishing such cases may help to refine the surgical treatment of mesial temporal lobe epilepsy.

1 Department of Neurological Surgery, Columbia University Medical Center, NewYork, NY 10032, USA
2 Department of Neurology, Columbia University Medical Center, NewYork, NY 10032, USA
3 Department of Neurosurgery, University of Utah, Salt Lake City, UT 84132, USA
4 Department of Neurosurgery, Baylor College of Medicine, Houston TX 77030, USA
5 Biosciences Institute, Newcastle University, Newcastle upon Tyne NE2 4HH, UK

Received March 05, 2023. Revised June 30, 2023. Accepted July 19, 2023. Advance access publication August 3, 2023
© The Author(s) 2023. Published by Oxford University Press on behalf of the Guarantors of Brain. All rights reserved. For permissions, please e-mail: journals.permissions@oup.com

Correspondence to: Catherine A. Schevon, MD, PhD
Department of Neurology, Columbia University Medical Center, 710 W 168th Street, 7th floor, New York, NY 10032, USA
E-mail: cas2044@cumc.columbia.edu

Keywords: single unit; inhibition; ictal recruitment; interneurons; ictal territories

Introduction

Understanding the neuronal dynamics of seizure genesis and spread are important to efforts being made to improve the medical and surgical management of epilepsy. While surface and intracranial EEG can provide valuable localizing information, they are relatively insensitive to neuronal firing activity; indeed, similar appearing EEG features may be associated with very different patterns of unit activity. Previously, we described a dual-territory seizure structure, in which a core of intense neural firing that drives the seizure can be distinguished from the relatively large 'penumbra' in which neural firing is inhibited.[1-8] This is consistent with observations of intense, synchronized neuronal firing following the ictal transition from *in vitro* studies.[6,9-11] Conversely, others have proposed that seizures arise from the aggregate activity of pathological diffuse networks,[12-14] based on observations of modest, heterogenous firing rate changes.[15-22] However, our prior work was limited due to relatively small study populations with a variety of epilepsy syndromes, and being confined to neocortical onsets, which may show different cellular activity to the hippocampal seizures that have been the focus of much prior animal and human work.[20,22-27]

A significant issue affecting all such studies is the lack of a gold standard for identifying the cellular activity that defines the ictal transition. Attention has focused on the role of fast-spiking interneurons, with animal studies and a recent study in human mesial temporal structures demonstrating increased fast-spiking interneuron firing rates prior to the ictal transition,[28-30] and activating these cells optogenetically can induce seizure-like events *in vitro*.[31,32] An independent human study, however, demonstrated decreased interneuronal firing rates just prior to hippocampal ictal invasion from a neocortical source.[33] We hypothesized that the observed early ictal interneuronal firing patterns depend on the nature of local seizure involvement, which can be characterized by aggregate EEG and neuronal firing patterns. Here, we used multi-scale neuronal activity patterns, recorded using stereo-electroencephalography (sEEG) incorporating microwires, in patients undergoing surgical evaluation for pharmacoresistant epilepsy, to distinguish different ictal territories. In this way, we can identify cell-type specific neuronal firing patterns within a well-defined clinical and spatial context.

Materials and methods

Human recordings

Patients undergoing stereotactic depth electrode placement for presurgical evaluation of intractable focal epilepsy were simultaneously implanted with 'Behnke–Fried' type arrays, which consist of eight macroelectrodes, with eight microelectrodes protruding from the tip of the array (Ad-Tech Medical; Fig. 1G). Research was conducted under the oversight of Columbia University's Institutional Review Board; all patients provided informed consent prior to implant. The recording details were as described in our prior publication.[3] Macroelectrodes were localized using iELVis with co-registered postimplant CT and preimplant T_1 volumetric MRI scans.[34] Clinical determinations of the epileptogenic zone (EZ), consisting of the seizure onset zone (SOZ) and path of spread, as well as seizure semiology classification, were made by treating physicians and confirmed by a qualified epileptologist (C.A.S.) prior to analysis.

Data processing

Processing and analyses were performed using custom code written in MATLAB (MathWorks, Natick, MA). Analysis focused on microelectrodes and only the nearest viable macroelectrode ('macro-micro pair'). In a single instance, the recording quality necessitated the use of the second closest macroelectrode (Patient 13). Microelectrode and macroelectrode signals were de-meaned, then common average re-referenced. The macroelectrode signal was processed into two data streams using symmetric 512th-order finite impulse response (FIR) bandpass filters: a low frequency (2–20 Hz) band capturing the dominant ictal rhythm and a high-gamma band (80–150 Hz) as a proxy for population firing.[35-37] To quantify interictal high-frequency oscillation (HFO) rates for each macro-micro pair, HFOs were detected from 10-min sleep epochs using RIPPLELAB,[38] with visual review to exclude false positives, following published guidelines.[39] Multi- and single-unit activities were isolated from the 300 Hz–5 kHz band from each microelectrode recording as previously described.[3] Briefly, after artefact removal, extracellular action potentials were detected and clustered into single units in the 5-min pre-ictal period. Units were then tracked through the seizure using a probabilistic template-matching algorithm[3] to minimize loss of units due to obscured clustering or waveshape deformation that could erroneously give the impression of reductions in firing rates. Only macro-micro pairs with isolatable single-unit activity were included.

Analyses focused on two epochs: a 5-min period prior to seizure onset ('pre-ictal') and an 'ictal' period from seizure onset until the start of either a pre-termination pattern as described previously[35] or, in the case of focal to bilateral tonic-clonic seizures, the time of transition to tonic-clonic semiology [identified by expert review of video EEG (C.A.S.)]. Both the tonic-clonic phase and pre-termination stage—characterized by irregular inter-discharge intervals and reduced per-discharge high-gamma activity—feature unique spatiotemporal dynamics[35,40-42] and were excluded from the analysis.

Neuronal activity metrics

To assess seizure-related neural patterns, we used metrics designed to capture relevant multiscale features from each microelectrode and nearest macroelectrode. Up to three electrographic seizures per patient with units trackable across the ictal transition were studied (Supplementary Table 1). The following metrics were used: multi-unit firing rate (FR); multi-unit firing entrainment to the low frequency rhythm (MU-E); unit waveform width (full-width at

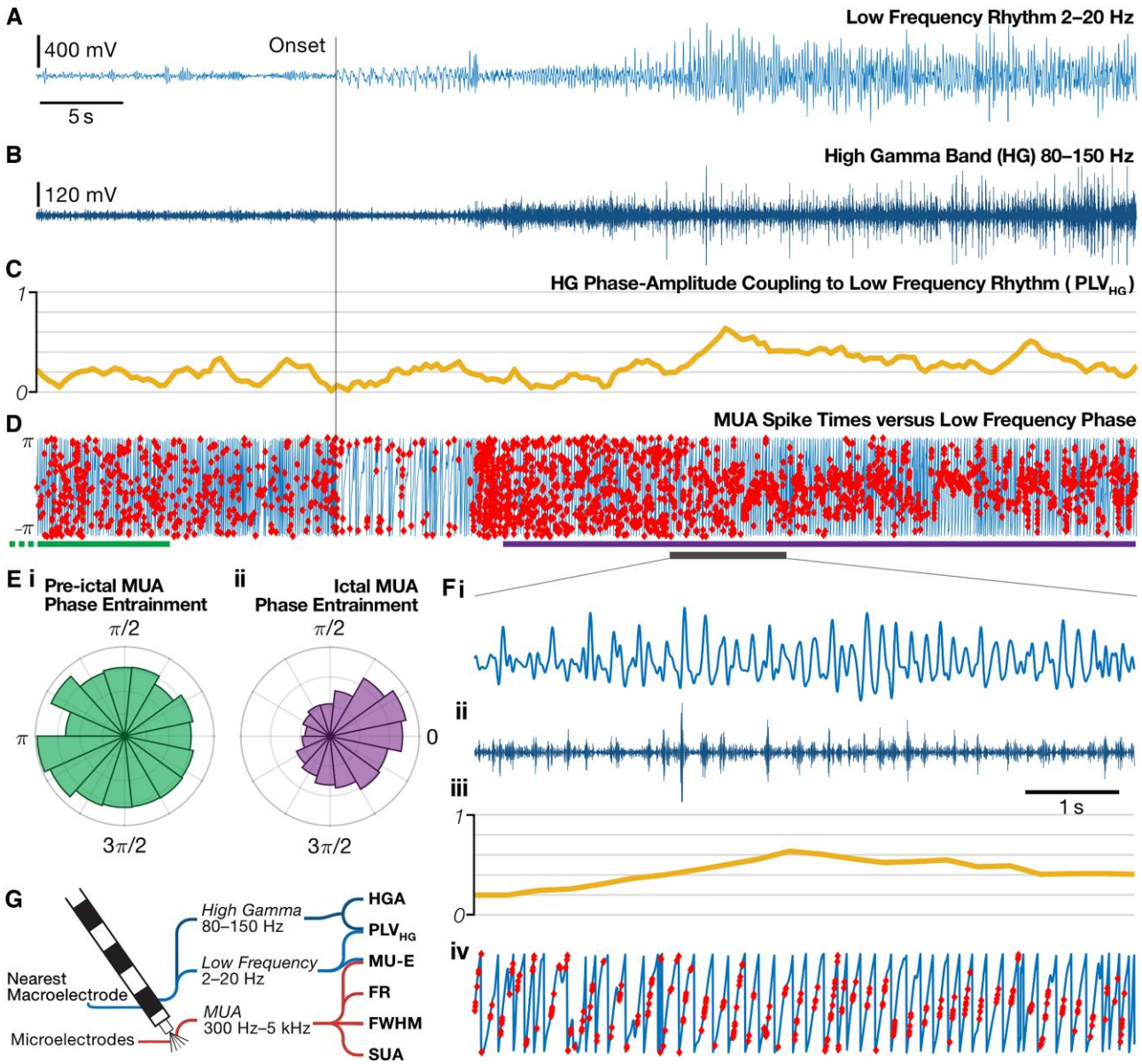

Figure 1 Illustration of neural activity metrics. The raw signal obtained from the nearest macroelectrode is filtered into two bands: the 2–20 Hz low frequency rhythm (**A**) and the 80–150 Hz high-gamma band (**B**). (**C**) The coupling between the high-gamma amplitude and the low frequency phase (phase locking value, PLV_{HG}) can then be calculated across these signals obtained from the nearest macroelectrode. (**D**) Detected multi-unit spikes (red dots) from the microelectrodes provide firing rate and multi-unit entrainment (MU-E) to the phase of the low-frequency rhythm (blue line). (**E**) Polar histograms for the phases of all multi-unit spikes from the regions marked in **D**, comprising the same number of spikes in each of the pre-ictal epoch (**i**, green, starting prior to region plotted) and the ictal epoch (**ii**, purple), with corresponding Rayleigh z-statistic values of 2.90 and 107.3, respectively. (**F**) Expanded section from **A**–**D** as marked by the grey bar. (**G**) Schematic of 'Behnke–Fried' style electrode design and sources of data used in the above metrics. These are derived from recordings from microelectrodes, positioned at the distal end of the electrode shaft, and the distal macroelectrode on the same shaft. FR = multi-unit firing rate; FWHM = full-width at half-maximum; MUA = multi-unit activities; SUA = single-unit activities.

half-maximum, FWHM); macroelectrode high-gamma (80–150 Hz) amplitude (HGA); and high-gamma phase-amplitude coupling to the low frequency rhythm (phase locking value, PLV_{HG}; Fig. 1). FR, FWHM and HGA were calculated as the ratio of their ictal and pre-ictal values. MU-E was calculated by extracting the instantaneous phase of the low-frequency signal from the nearest macroelectrode at each multi-unit spike time captured on the microelectrodes and calculating the Rayleigh z-statistic. HGA was determined using the envelope of the Hilbert transform on the high-gamma filtered signal from the nearest macroelectrode. The PLV_{HG} was then computed from the Hilbert-transformed high-gamma signal to the phase of the low-frequency rhythm using 3-s sliding windows every 333 ms,[43-45] then averaged for the ictal epoch.

Dimensionality reduction and electrode cluster analysis

To ensure metrics across all recordings approximated a normal distribution for comparative purposes, each was Box–Cox transformed[46] prior to analysis in feature space. T-distributed stochastic neighbour embedding (t-SNE) was used to visually assess groupings

among macro-micro pairs. Principal component (PC) analysis was used to validate the presence of clusters in the dataset.

To determine the optimal number of clusters in the PC space, successive k-means solutions were calculated and evaluated using the Calinski–Harabasz index. Solutions with Calinski–Harabasz values with <1% probability of being observed in a null dataset, created by randomly shuffling the distances between observations in the PC space and recalculating the Calinski–Harabasz index over 1000 runs, were also evaluated for cluster stability (Jaccard coefficients >0.6)[47] using bootstrap resampling (R 'fpc' package clusterboot function).[48,49]

The relative contribution of each metric to PC clustering was calculated by summing the product of the variance explained for a given PC by the metric coefficients for that PC, then dividing the result by the sum of coefficients for a given metric across all PCs. Cluster centre separation was calculated via Hotelling's two-sample T^2 test on Mahalanobis distances, with a Bonferroni–Holm-corrected F-test to determine statistical significance.[50]

Single metric comparisons

The original, non-Box–Cox transformed data for each metric was compared between clusters using a two-tailed Wilcoxon rank-sum test with Bonferroni–Holm correction for multiple comparisons. Line-length served as a quantitative proxy for the clinically determined EZ.[51,52] The interictal HFO rates between clusters was compared using a two-sample t-test.

Single-unit putative cell-type classification

Single units were subclassified into putative fast-spiking (FS) and regular-spiking (RS) cell-types based on waveform shapes and cell-intrinsic metrics. For each unit, the mean waveform was calculated as the spike-triggered average from the raw, unfiltered original signal, z-scored and a two-component Gaussian mixture model was fitted to the z-scored waveform's scores in PC space, which has been shown to separate FS interneurons from the RS population.[53] FS cells primarily represent PV^+ interneurons due to their fast hyperpolarization via $K_v3.1/K_v3.2$ channels,[54,55] i.e. roughly 40% of interneurons,[56] resulting in the remaining RS cells comprising a mixture of predominantly excitatory and a minority of inhibitory cells. To extract putative inhibitory cells from the RS population, the autocorrelation for each unit that was not already classified as a FS interneuron was fitted with a set of exponentials using the 'fit_ACG' function from 'CellExplorer'.[57] The τ_{rise} exponential fit captures the timing of the rise in probability of following action potentials occurring after an initial spike from that neuron, a feature which can separate pyramidal cells from non-FS interneurons, due to their cell-intrinsic firing dynamics.[57,58] We fitted a two-component Gaussian mixture model to the τ_{rise} values across all RS units, providing probabilities for the subclassification of each RS cell as inhibitory ('RS interneuron') or excitatory.

To assess the expected proportion of action potentials that may have been subthreshold at any given moment, the distribution of the unit's voltage at detection was fitted with a Gaussian,[59] and to account for any drift, that Gaussian was shifted such that its mean was equal to the smoothed spline of voltages through time ($\lambda = 0.001$; weighted by match confidence[3]) at any given time-point. The cumulative probability of this shifted Gaussian that was below the original threshold used for spike detection provides an estimate of the rate of missing spikes for each unit. Cessations of firing were calculated as the moment the ictal firing rate dropped to zero or <−3 SD of the pre-ictal rate, whichever was lower (to prevent low-firing-rate units from the pre-ictal epoch that reduced to zero by chance being deemed cessations), and their probabilistic firing rate had to remain confident that no action potentials occurred for the rest of the seizure (i.e. <50% chance of a single spike continuously).

For statistical analyses of single-unit firing patterns, a Kolmogorov–Smirnov test for normality was calculated for the comparison groups, and if all were normally-distributed an unpaired t-test was used, otherwise the non-parametric Mann–Whitney U-test was used.

Results

Recordings from 34 seizures across 19 patients had isolatable single units in the peri-ictal period (Supplementary Tables 1 and 2; 10 females; 19–55 years old), with 156 single units across 52 microwire arrays total, averaging 2.7 arrays per patient (range 1–4).

Clustering of ictal neuronal activity metrics demonstrates up to three distinct patterns

Neural activity metrics during seizures were computed for each microelectrode and nearest macroelectrode (see 'Materials and methods' section). Each seizure may be represented by multiple macro-micro pairs, i.e. multiple recording locations (Supplementary Table 2), and each macro-micro pair was treated as its own entity for analysis of activity patterns. Dimensionality reduction with t-SNE revealed the visual presence of two to three robust groups (Fig. 2A). However, since t-SNE is not in itself reliable for clustering,[60] principal component analysis (PCA) with k-means clustering was used to analyse these groupings. The first four PCs explained >99% of the variance within the data and all subsequent analyses were conducted across these components.

The PCA results were found quantitatively to contain more than one cluster ($P < 0.001$; Duda–Hart[61] test). Clustering solutions that were likely to have arisen by chance ($k = 4$–6), were unstable[47] ($k = 7$) or produced clusters with only single members ($k > 7$) were excluded from further analysis, leaving $k = 2$–3 (Fig. 2B and C). The two-cluster solution was considered optimal as it maximized the Calinski–Harabasz index[62] (Fig. 2B), while the three-cluster solution identified a subcluster within one cluster of the two-cluster solution (explored in detail later).

We sought to characterize each metric's contribution to the optimal clustering seen in PC space in order to quantify its potential for localization. PLV_{HG} explained 45.66% of the variance across the first four PCs, followed by MU-E, FR, HGA and FWHM (21.40%, 19.55%, 10.01% and 3.11%, respectively). To assess for robustness and ensure that the two-cluster separation was not due to any one feature, we re-ran the PCA using a leave-one-out analysis, while maintaining cluster assignments from the original two-cluster solution: cluster centre separation remained significant in each metric's absence ($P < 0.05$ in each, Bonferroni–Holm-corrected F-test; F-value for each: PLV_{HG}-excluded = 5.08; HGA-excluded = 105.61; FWHM-excluded = 105.60; FR-excluded = 94.13; MU-E-excluded = 107.92). The strongest metrics for grouping the data were those based on entrainment of higher frequency activity to the ictal rhythm: PLV_{HG} followed by MU-E, more so than their underlying firing rate or signal amplitude without respect to the ictal rhythm.

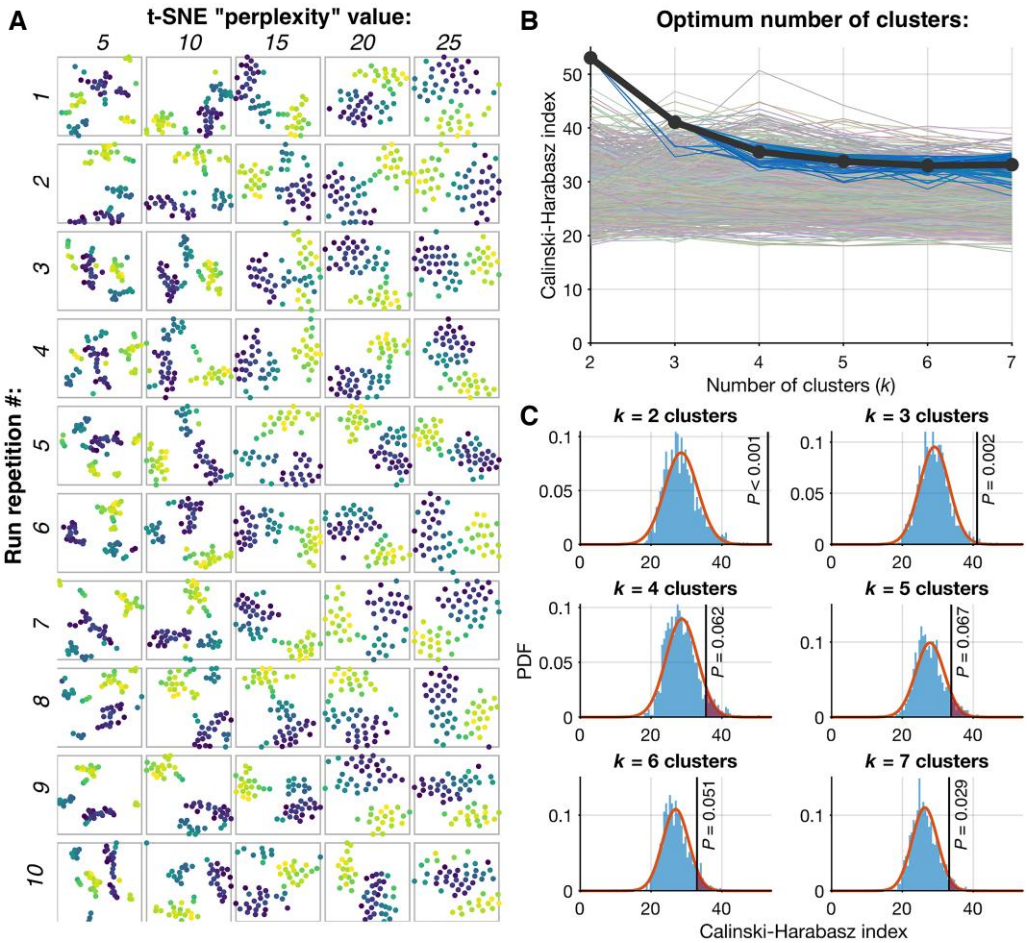

Figure 2 Distinct neural activity patterns identified with clustering techniques. (**A**) Each macro-micro pair's metrics plotted in feature space after dimensionality reduction (t-distributed stochastic neighbour embedding, t-SNE), revealing two to three visually distinguishable clusters across multiple runs and different 'perplexity' values, where perplexity is a tunable parameter that, roughly, sets a target number of neighbours for each cluster centre.[83] For ease of interpretation, each data-point is colour-coded based on the results of an average run (run 6; perplexity = 15). (**B**) To derive null distributions for Calinski–Harabasz (CH) indices that would arise by chance, principal component scores between data points were randomly shuffled and the CH index recalculated 1000 times (faded multi-coloured lines in background). The CH index is then calculated on the original data 100 independent times (blue lines), and the final CH index is calculated as the mean of those runs (thick black line). (**C**) Gaussian curves (orange) are fitted to the null distributions found in **B** (blue), from which the probability of finding a value as extreme as the observed CH index (black line) can be calculated. While $k = 7$ was unlikely to arise by chance, the solution was unstable (see 'Materials and methods' section). Individual clustering solutions can be seen in Supplementary Fig. 1.

Distinguishing activity patterns of recruited tissue

A single cluster, identical across both solutions, closely resembled neuronal firing patterns previously associated with the ictal core[1,3,5,43] (Figs 3A and 5A), so we hypothesized that this cluster represented recruitment, labelling it 'R'. Of the 20 macro-micro-electrode pairs clinically determined to be in the EZ, all but one were members of this group ($P < 10^{-4}$, Fisher's exact test). The remaining cluster was labelled non-recruited (NR; sub-grouped as NR_1 and NR_2 in the derivative three-cluster solution). Macro-micro pairs in R demonstrated larger values compared to pairs in the NR cluster for all five metrics used in the cluster analysis (Fig. 3B; R > NR, Bonferroni–Holm rank-sum $P < 0.05$ in each), consistent with predicted characteristics of recruited tissue.[1-5] Line-length, a control metric as a proxy for visual EEG but not used in clustering, was similarly higher in R (Fig. 3B; $P < 0.05$, Bonferroni–Holm rank-sum).

To assess this designation independently from the data used for clustering we contrasted interictal HFO rates between groups using semi-automated HFO detection on 10-min interictal sleep recordings, given the association between HFOs and seizure source regions.[38,63,64] HFOs (80–600 Hz) were detected in 11% of macroelectrodes (2/18) in NR versus 71% (10/14) in R ($P = 0.00047$, chi-square test), all in hippocampal electrodes. Greater rates were found in contacts from R compared to NR both for HFOs (13.3 ± 16.1 HFOs/10 min versus 0.8 ± 3 HFOs/10 min; $P = 0.016$, unpaired *t*-test) and fast ripples (5.8 ± 8.0 fast ripples/10 min versus 0.2 ± 0.7 fast ripples/10 min; $P = 0.027$, unpaired *t*-test).

Despite the overall group differences, there was considerable overlap in most metrics—only phase-locking of high-gamma activity to the ictal rhythm (PLV_{HG}) was able to discriminate the two groups without overlap between their distributions [Fig. 3B(v)]. Similarly, PLV_{HG} displayed temporal stereotypy during each seizure (Fig. 3C), indicating an evolution from non-recruited to recruited status at these territories. To further explore this, we fitted a Gaussian mixture model to the two metrics accessible to routine clinical recordings (PLV_{HG} and HGA), in order to derive instantaneous probabilities of each location being recruited at any given time (Fig. 4). Doing so revealed that recruitment always arose from NR feature-space (Fig. 4B–F) and

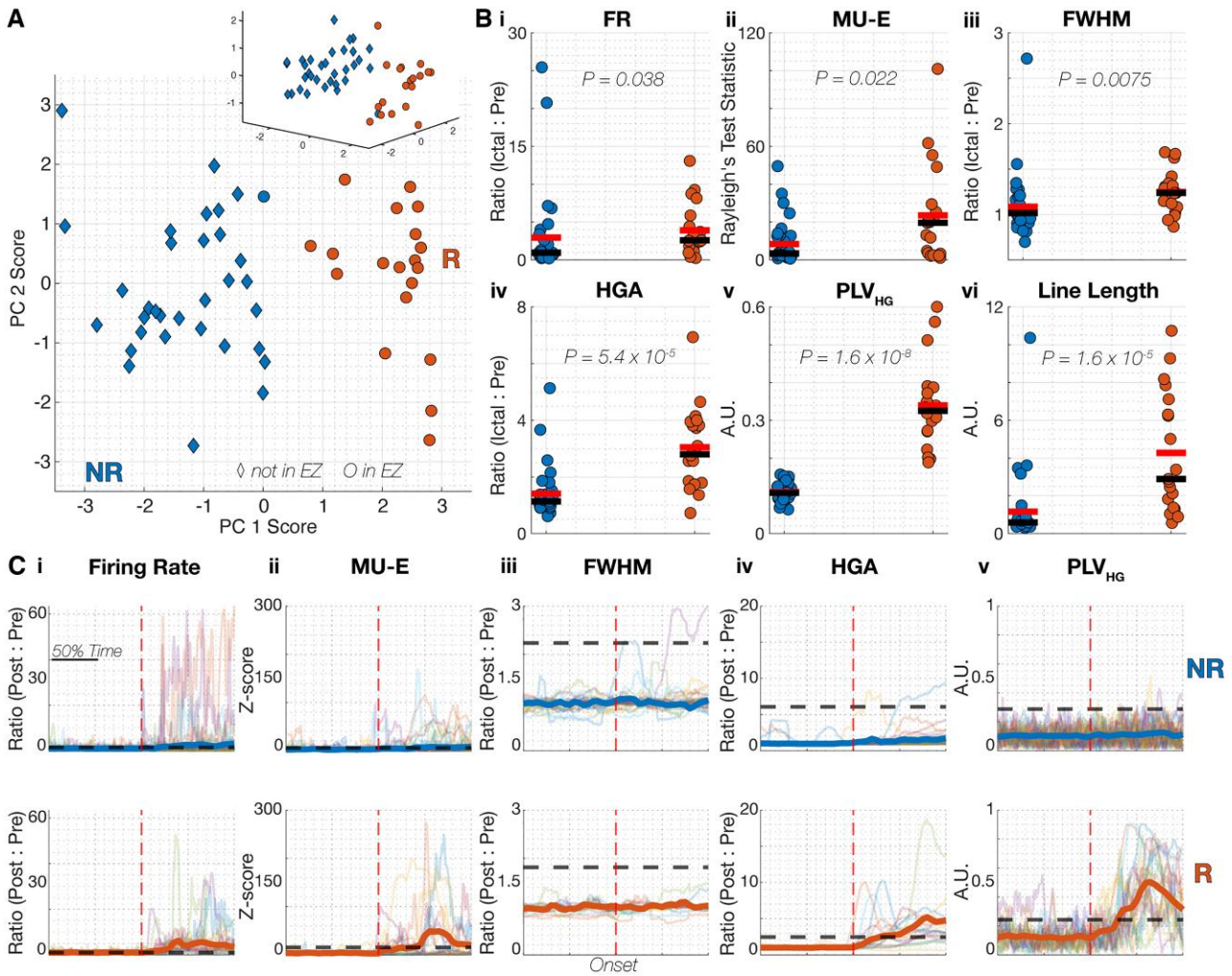

Figure 3 Ictal activity patterns revealed by the two-cluster solution. (**A**) Principal component analysis (PCA) results colour coded by group (blue = non-recruited; orange = recruited); all but one clinically determined epileptogenic zone (EZ) site corresponded to the recruited group. (**B**) Box plots comparing each metric by group (red and black bars: mean and median, respectively). Line-length is shown as a quantitative proxy for the clinically determined EZ and was not included in the dataset used for PCA. Note that while all metrics showed significant differences between groups, complete separation was apparent only for the phase locking value (PLV_{HG}; Bv). (**C**) The trajectory for each macro-micro recording in a given seizure (faded lines) with group means overlaid (thick lines) for each metric, aligned to seizure onset (red dashed line). Data are plotted against 'normalized time' to facilitate comparison (time for each data-point was divided by that seizure's duration). Black-dotted lines represent 2.5 SD above the pre-ictal mean for each metric. Note how consistently PLV_{HG} changes across the ictal transition for each member in their respective groups (Cv): by about halfway through the ictal period ('50% time') the average PLV_{HG} across members in the recruited group was more than 2.5 SD above the pre-ictal average, whereas ictal PLV_{HG} is unchanged from pre-ictal baseline for each member in the non-recruited group. FR = multi-unit firing rate; FWHM = full-width at half-maximum; HGA = high-gamma amplitude; ME-U = multi-unit entrainment.

followed stereotyped paths across seizures prior to recruitment (Fig. 4D) and once recruited (Fig. 4E and F).

Differences between groups were not explained by differing ictal durations (NR mean: 43 s, range: 18–198; R mean: 37 s, range: 13–66), nor in the proportions of seizure types or mesial temporal versus lateral temporal onsets, although the proportion of extra-temporal onset zones was higher in NR [Supplementary Table 2; 48.5% (16/33) and 10.5% (2/19) in NR and R, respectively; $P = 0.014$, chi-square]. Differences were not due to patient- nor seizure-specific patterns: seizures from four patients (Patients 4, 5, 8 and 10) included simultaneous recordings across anatomical sites that were classified into different groups within the same seizure, and in three cases the same contacts were classified into different groups across seizures (Patients 4, 11 and 12; Fig. 4, Supplementary Table 2 and Supplementary Fig. 2).

Hippocampal electrodes were evenly distributed between groups (NR = 14/33; R = 14/19), while the remainder of recordings were predominantly from cingulate (NR = 18/33; R = 3/19; Supplementary Table 2). For the 14 recruited hippocampal recordings, the SOZ was proximal: ipsilateral mesial temporal in 11 and ipsilateral neocortical temporal with later spread to hippocampus in 3. In contrast, for hippocampal recordings in NR, the SOZ was not ipsilateral mesial temporal in any, instead being ipsilateral, extratemporal neocortical for eight, contralateral mesial temporal for two and contralateral neocortical for four (Supplementary Table 2).

The NR group was further subdivided in the three-cluster solution (Fig. 5A; 'NR_1' and 'NR_2'). Unlike the R/NR distinction, these sub-groups were not distinguishable by PLV_{HG} [Fig. 5B(v); Bonferroni–Holm-corrected rank-sum $P = \sim 1$], nor line-length (a quantitative proxy for visual EEG assessment; $P = 0.91$). However, differences in measures reflecting population firing activity (HGA, FR, MU-E and FWHM) distinguished the two (Fig. 5; $P < 0.05$ in each, Bonferroni–Holm-corrected rank-sum). In general, ictal firing

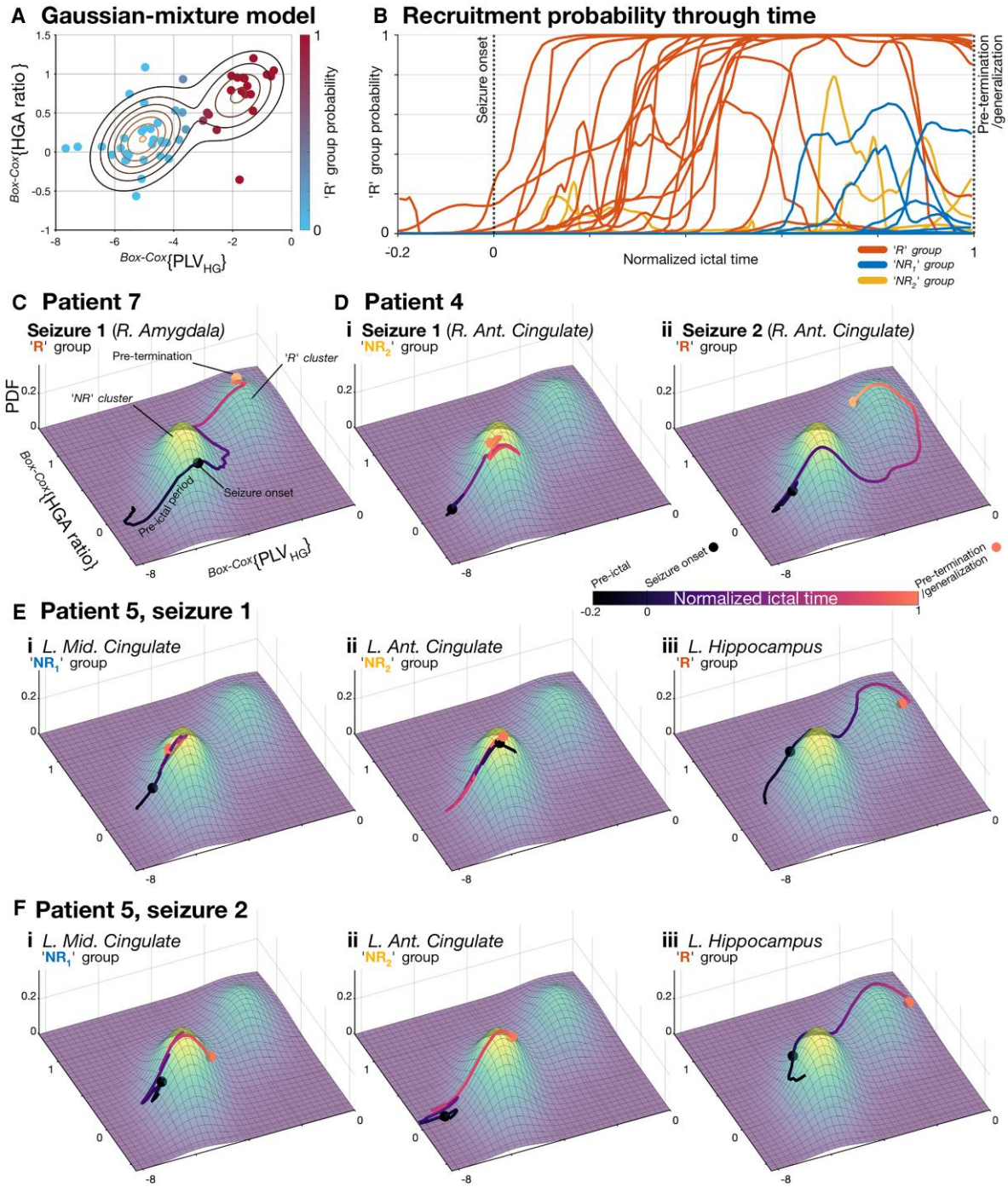

Figure 4 Recruitment follows a trajectory starting in the non-recruited feature space. (**A**) Fitting a Gaussian mixture model to the Box–Cox transformed macro-electrode metrics can provide probabilities of belonging to the recruited versus non-recruited groups for any given value. (**B**) The instantaneous probability of being in recruited tissue for each electrode, throughout the pre-ictal and ictal epoch (normalized time), based on the continuous phase locking value (PLV_{HG}) and high-gamma amplitude (HGA) values for each seizure. Traces are colour-coded by original clustering group [recruited (R) in orange; non-recruited (NR_1) in blue and NR_2 in yellow], showing the rise in probability that the tissue recorded in the 'R' group has transitioned to recruited as the seizure progresses, arising from a non-recruited state. Note that while a subset of 'NR' recordings show late increases in recruitment probability, the majority remain below 50%, i.e. are still deemed more likely to be unrecruited than recruited. Only two transiently surpass 50% probability, while all in the 'R' group reach 100%. (**C–F**) Example trajectories of a single electrode and seizure in the feature space from **A**, colour-coded by normalized ictal time, with seizure onset and pre-termination marked with circles. Heat map below shows the probability density function, revealing the dense regions for 'NR' and 'R' values. (**C**) Recruited electrode site with trajectory starting in the non-recruited region and progressing to the 'recruitment' feature space. (**D**) A single electrode site that remained unrecruited in seizure 1 (**i**, focal unaware seizure) and then became recruited in seizure 2 [**ii**, focal to bilateral tonic-clonic (FTBTC) seizure]. Note the similar trajectory in seizure 2 prior to transitioning to recruitment. (**E** and **F**) Three paired electrodes from two seizures in the same patient, showing stereotypy of trajectory across seizures for each electrode, but dissimilar trajectories between different electrode sites: (**i**) mid-cingulate electrode that remained in NR_1 throughout both seizures; (**ii**) an anterior cingulate electrode that remained NR_2 in both; and (**iii**) a simultaneously recorded hippocampal electrode that transitioned from not-recruited to recruited during the seizure while the others remained unrecruited.

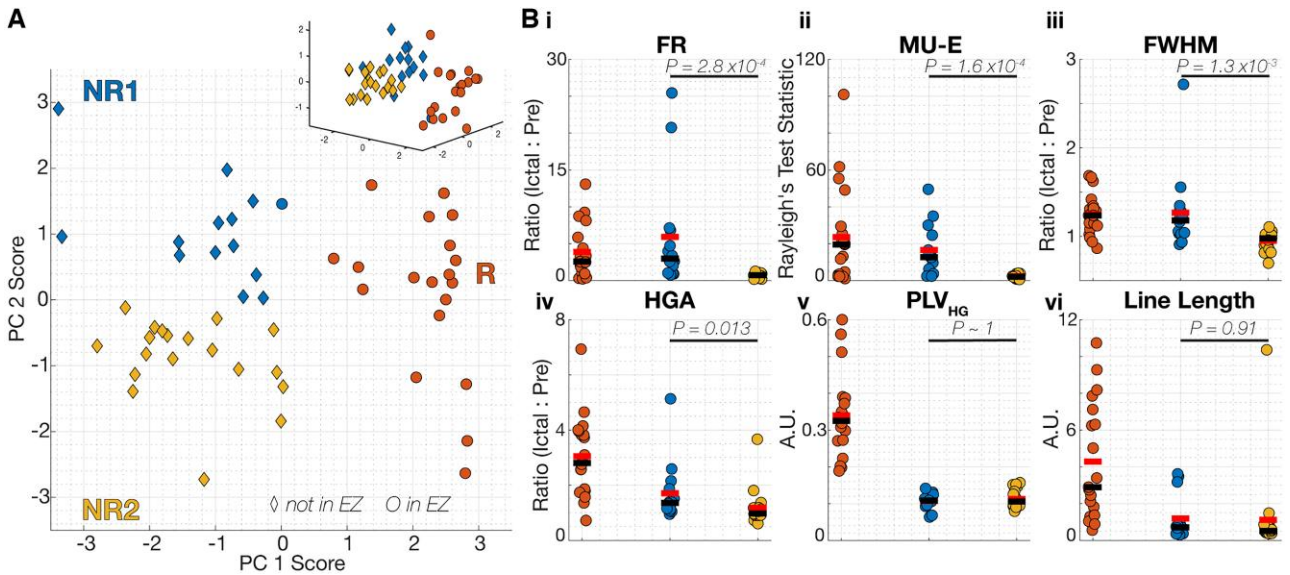

Figure 5 The three-cluster solution reveals a subgroup of electrodes within the non-recruited group. (**A**) Data plotted as in Fig. 3, but colour-coded to demonstrate the three-cluster solution. The third cluster represents a subgroup of macro-micro pairs within the non-recruited group termed NR_1 (blue) and NR_2 (yellow). The recruited group (R) is the same in both the two- and three-cluster solution. (**B**) Data plotted as per Fig. 3B but with subgroups NR_1 and NR_2 isolated. Only comparisons between the subgroups are made to compare ictal activity pattern. Compared to NR_2, subgroup NR_1 displayed significantly greater values in all metrics except for the phase locking value (PLV_{HG}) and line-length. FR = multi-unit firing rate; FWHM = full-width at half-maximum; HGA = high-gamma amplitude; MU-E = multi-unit entrainment.

patterns in NR_1 more closely resembled recruited tissue than did those in NR_2, though without the phase-locking to the dominant ictal rhythm indicative of local recruitment into seizure-driving tissue. Marked increases and decreases in firing rate during the seizure was observed in all groups. The heterogeneity in R differed from our prior neocortical studies, so we explored this further using single-unit analysis.

Single-unit analysis reveals cluster and cell-type differences in neuronal activity patterns

Individual single units ($n = 156$ units, 34 seizures, 19 patients) were probabilistically subclassified as excitatory and inhibitory cells, based on waveshape (fast-spiking; FS interneurons) or subsequently via autocorrelation (RS interneurons; see 'Materials and methods' section).[57] Seventeen and 21 units (10.90% and 13.46%) were classified as FS and RS interneurons, respectively, at a confidence threshold of 50%; this classification was stable: restricting to a 95% confidence threshold reduced these numbers minimally (15 and 18 in total; 9.62% and 11.54%; Supplementary Fig. 3). A cut-off of 50% likelihood was therefore used for all categorical analyses by cell-type.

In contrast to the results for multi-unit firing, which includes all identifiable action potentials, ictal single-unit firing rates tended to decrease. Firing rate reductions were seen in 69.2% of single units, with 24.4% demonstrating decreases greater than 3 SD from pre-ictal firing rates (Fig. 6A). Firing rate increases exceeding pre-ictal baseline by 3 SD were seen in a minority (5.1%) of single units. No difference was found between recruited and non-recruited groups overall ($n = 49$ and 107 units, respectively; $P = 0.59$, unpaired t-test) or by cell-type [$P = 0.13$ and 0.56; excitatory ($n = 38$ and 80) and inhibitory ($n = 11$ and 27) cells, respectively; unpaired t-test]. Overall, there was a trend towards larger decreases in firing rates of inhibitory compared to excitatory neurons during the seizure (Fig. 6B; $P = 0.065$; unpaired t-test). When separated by groups, however, the excitatory population was less impacted than inhibitory cells in the non-recruited group (Poisson-derived z-score mean ± SD: -0.79 ± 2.09 versus -2.28 ± 3.77, respectively; $P = 0.012$, unpaired t-test). Meanwhile, decreases were equivalent across cell-types in the recruited group (-1.36 ± 5.76 versus -1.46 ± 2.51, inhibitory and excitatory cells, respectively; $P = 0.93$, unpaired t-test). These changes were similar across contacts in SOZ versus those in regions of spread (-1.10 ± 2.83 versus -1.38 ± 5.32, respectively; $P = 0.220$, rank-sum); however, regions of spread showed higher variance ($P = 0.020$, Ansari–Bradley test). Within the non-recruited subgroups, interneuronal firing rate remained reduced in NR_1 ($P = 0.0058$, unpaired t-test), while in NR_2 both excitatory and inhibitory populations' firing remained minimally altered from pre-ictal rates ($P = 0.68$, unpaired t-test; Supplementary Fig. 5).

We next explored whether a subset of neurons ceasing firing entirely might explain the lack of overall increased firing rates associated with ictal invasion. Despite strict criteria for cessation (see 'Materials and methods' section; Fig. 6C) and the permissive template-matching, 34 units (21.8%) ceased firing entirely prior to pre-termination. The proportion of inhibitory neurons that became silent was higher in R than NR (5/11, 45.5% versus 2/27, 7.41%, respectively; $P = 0.0061$, chi-square test). Excitatory cells also demonstrated cessation of firing, though similarly across groups (26.3% versus 15.8% in NR and R, respectively; $P = 0.21$, chi-square test). The majority of these excitatory cessations were in NR_2 rather than NR_1 (35.3% versus 8.9%; $P = 9.13 \times 10^{-4}$, chi-square test; Supplementary Fig. 5).

To assess whether apparent firing cessations could be an artefact of spike detection methods, we tracked spike amplitude trajectories for each unit and determined the theoretical proportion of spikes that would be expected to be subthreshold for detection at any moment (Fig. 6C; see 'Materials and methods' section). Trajectories prior to cessation were variable (Fig. 6D; 60.9% and 36.4% decreasing in amplitude in NR and R, respectively; $P = 0.18$, chi-square test), although none had its mean amplitude reach

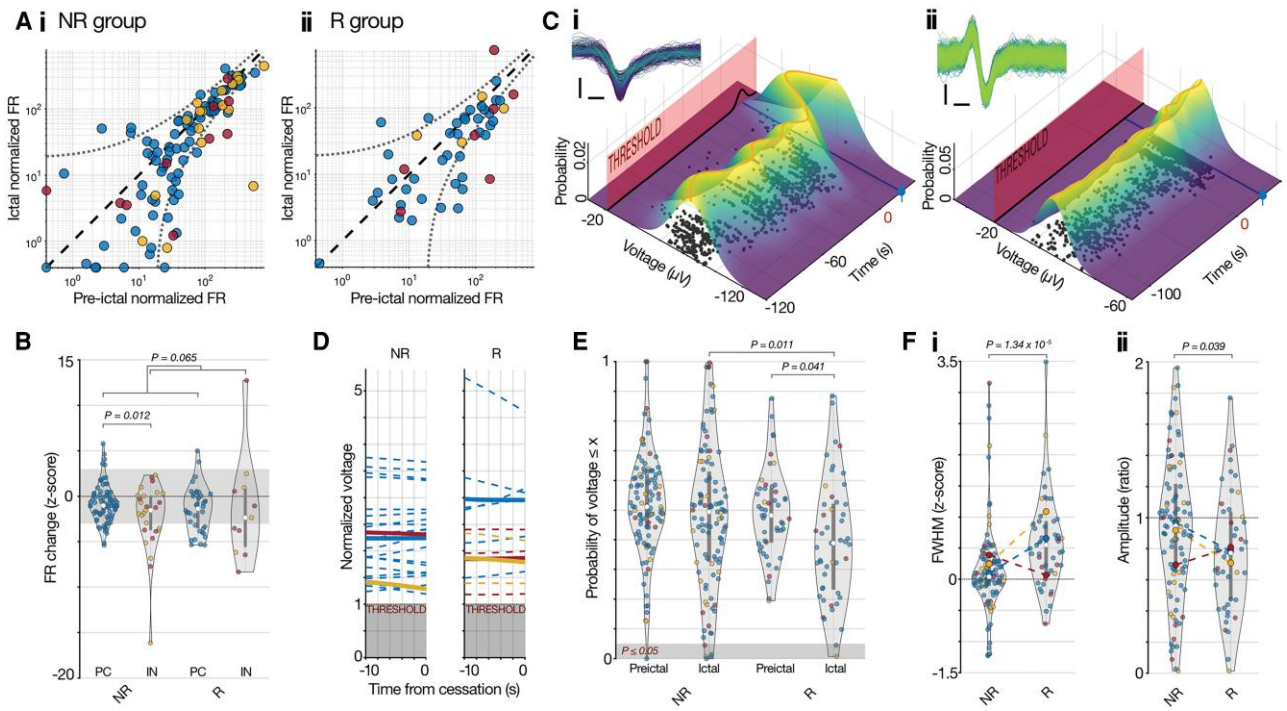

Figure 6 Single-unit ictal firing pattern analyses by putative cell-type. (**A**) Pre-ictal versus ictal normalized firing rates (FR) for pyramidal cells (blue), and interneurons [red: fast-spiking (FS); orange: regular spiking (RS); same colour-coding throughout figure] in non-recruited (**i**) and recruited (**ii**) groups. Firing rates were normalized to the ictal epoch duration to facilitate visual comparison across seizures; equivalent raw firing rates are shown in Supplementary Fig. 4. Dashed line: equal firing rates across epochs; dotted lines: ± 3 SD changes in a Poisson distribution for that firing rate.[84] Data on axes lines represent zero firing. (**B**)Violin plots of the ictal firing rates as calculated in **A**, z-scored by the Poisson-estimated SD by cell-type/group. Each dot is a single unit during one seizure. Shaded region: ± 3 SD change from pre-ictal rates. (**C**) Calculation of single-unit amplitude trajectories through time, showing an example of firing cessation (blue line and marker) with increased chance of undetected firing (**i**) and another with stable action potentials (**ii**). Orange line and heat map: fitted spline and instantaneous probabilistic amplitude distribution (see 'Materials and methods' section). Red barrier: threshold for spike detection. Black line: instantaneous probability of spikes from that neuron being undetected. Dots: spike time and voltage at trough (diameter: single-unit assignment confidence). *Inset*: All spike waveforms [scale bars = 0.2 ms, 50 μV (**i**) and 20 μV (**ii**); colour: spike time]. (**D**) Trajectories from fitted splines in 10 s prior to cessation, normalized to detection threshold. (**E**) Probability of that voltage or smaller for the mean of the fitted spline based on the pre-ictal distribution of voltages for each single unit. (**F**) Waveform metrics for each single unit, showing a population increase in spike duration (**i**) and decrease in amplitude (**ii**) in R, normalized to pre-ictal values for each unit. Note the inverse relationship in the FS interneuron population (red).

threshold. The proportion of spikes from each unit that was likely subthreshold at the moment of cessation was similar across both groups, and not sufficient to explain the detected cessations as artefactual [NR: 5.03% ± 9.97% (median: 0.03%) versus R: 3.71% ± 7.98% (median: 0.02%); $P = 0.94$, rank-sum]. To determine the impact of spike detection thresholds on firing rate calculations during the seizure, the same probabilistic method for the subthreshold proportion of spikes was calculated continuously, regardless of cessations (Fig. 6E). The average proportion likely to be subthreshold was similarly low in both groups [NR: 3.01% ± 10.62% (median: 0.06%) versus R: 2.67% ± 5.87% (median: 0.08%); $P = 0.85$, rank-sum]. Thus, neurons did not appear to stop firing due to depolarization block or to have undergone enough action potential waveform alterations to cause spike shapes to become undetectable.

Ictal recruitment by cell-type and territory

In neocortical recordings, increases in spike waveform duration and decreases in spike amplitude are thought to represent recruitment at the level of individual neurons.[3] Therefore, we assessed waveform alterations in each group identified in the previous analyses to determine its applicability in limbic structures. At the population level, spike duration was longer in the recruited versus non-recruited group [Fig. 6F(i); $P = 1.34 \times 10^{-5}$, rank-sum], with similar changes in excitatory cells ($P = 9.0 \times 10^{-6}$, rank-sum), reflecting the equivalent multi-unit increases. However, no difference was found in inhibitory neurons across groups ($P = 0.36$, rank-sum). On inspection, this apparent stability was comprised of dichotomous responses of the two putative types of inhibitory cell across the groups: RS interneurons trended in the same direction as the excitatory population ($P = 0.047$, unpaired *t*-test), while FS interneurons trended in the opposite direction, albeit at chance levels ($P = 0.474$, unpaired *t*-test), suggestive of feedforward inhibition mediated by PV^+ interneurons. Similar trends existed for amplitudes [Fig. 6F(ii)]. The larger changes in FS interneurons in the non-recruited group were dominated by subgroup NR_1 (Supplementary Fig. 5), in keeping with feedforward inhibition mechanisms, however these were at chance levels with low numbers of observations (0.67 ± 1.41 versus 0.04 ± 0.39; $n = 6$ and 4; $P = 0.56$).

Since a marked increase in firing followed by an abrupt decrease in FS interneurons, suggestive of depolarization block, has previously been associated with neocortical ictal invasion,[4,30] we sought to characterize the timing of FS interneuron firing rate alterations during the seizure. The aforementioned pattern was detected in only one of the seven FS interneurons in the recruited group (Fig. 7A; a transient increase >20 SD from pre-ictal levels based on a 5-s SD Gaussian convolution) while the remainder decreased firing without prior increases (Fig. 7B). In the non-recruited group,

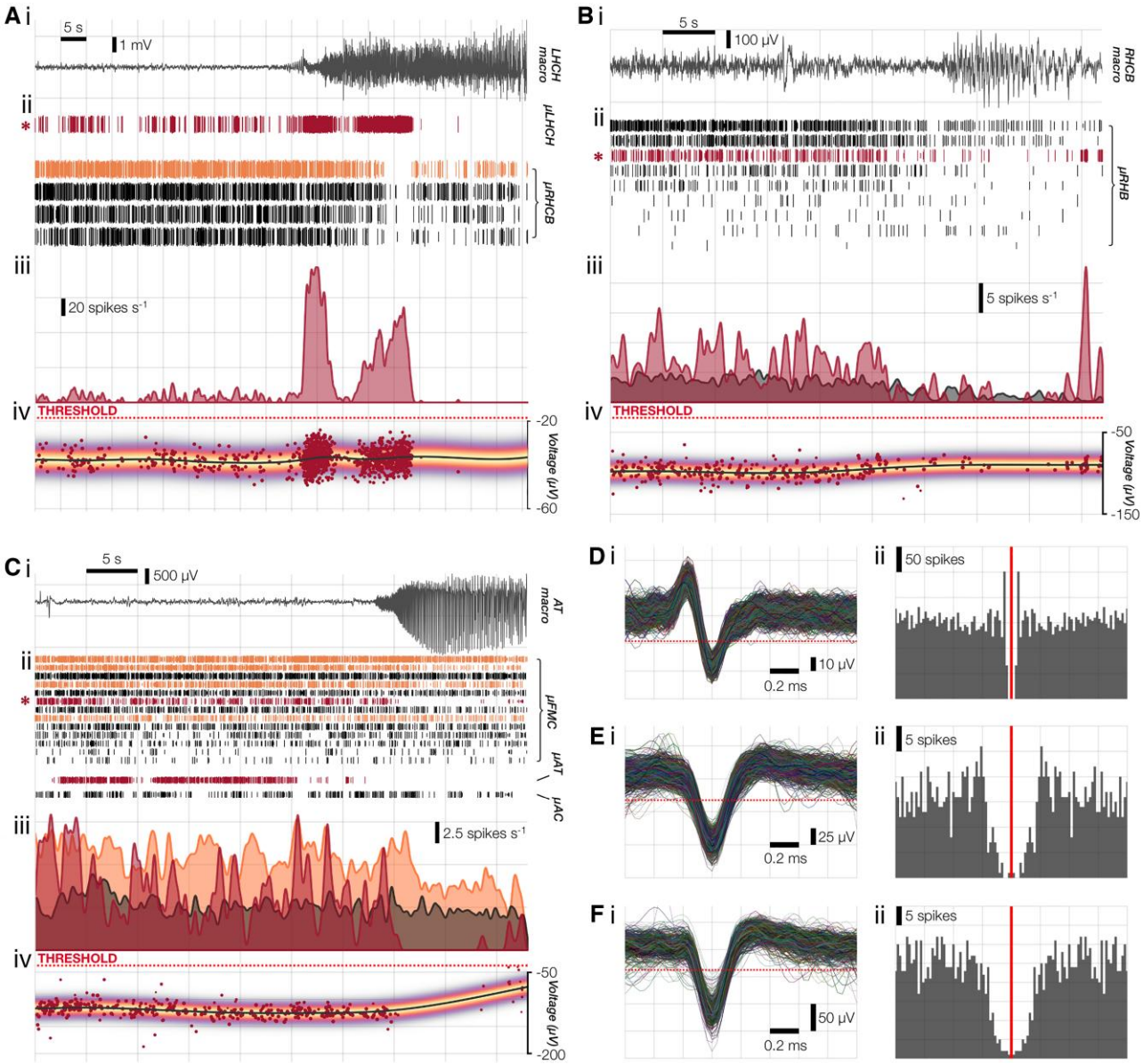

Figure 7 Example fast-spiking interneuron ictal firing patterns. (**A**) A transient increase followed by cessation in the recruited group. (**B**) A reduction of firing with no prior increase also in the recruited group. (**C**) A cessation with no prior increase in non-recruited group NR_1. (**i**) Local field potential from the labelled macroelectrode; (**ii**) paired raster plot of all units from each microwire bundle, showing putative pyramidal cells (black), regular spiking (RS) interneurons (orange) and fast-spiking (FS) interneurons (red). FS interneuron of interest is marked with an asterisk. Line height for each spike in the raster shows confidence each action potential arose from its assigned unit[3]; (**iii**) probabilistic firing rates for the marked FS interneuron along with the mean rates from other cells on the same microwire bundle [cell-type colours maintained from (**ii**)]; (**iv**) voltage at detection for each spike from the marked FS interneuron (red dots, size shows confidence of match to that neuron), with fitted spline (black line), instantaneous probabilistic distribution through time (heat map; see Fig. 6C), and threshold for detection (red dotted line). Note the stability and distance from threshold prior to each reduction or cessation of firing. (**D–F**) For the example FS interneurons in **A–C**, respectively: (**i**) Waveforms showing stability of waveshape and clearance from detection threshold (red dotted line); and (**ii**) autocorrelations over ±100 ms.

two of 10 FS interneurons transiently increased firing above 3 SD (both from the six FS interneurons in NR_1), while the remainder of the 17 total FS cells in the study decreased firing rate without any prior increases (Fig. 7C). Assessing transient increases over a range of detection parameters (i.e. analysing the full population without limiting to cells that reached a threshold) found FS interneuron firing rate increases lasted longest in NR_1, followed by R, in contrast to other cell-types where increases were dominant in recruited tissue (Supplementary Fig. 6).

Lastly, we sought to characterize changes in intrinsic firing patterns during seizures. The dissimilarity in the autocorrelations for each unit (Figs 8A and B; 'AC_{dist}'; see 'Materials and methods' section) showed a larger change in R than NR (0.22 ± 0.17 versus 0.13 ± 0.09; $P = 0.01$, unpaired *t*-test; Fig. 8C). While AC_{dist} captures shifts in the temporal pattern of firing, it is ambiguous as to the specific direction of the alteration, so we examined both the average autocorrelations by cell-type (Fig. 8D) and the magnitude of 'increases' in AC_{dist} ('AC_{dist}+', rather than absolute deviation) to characterize

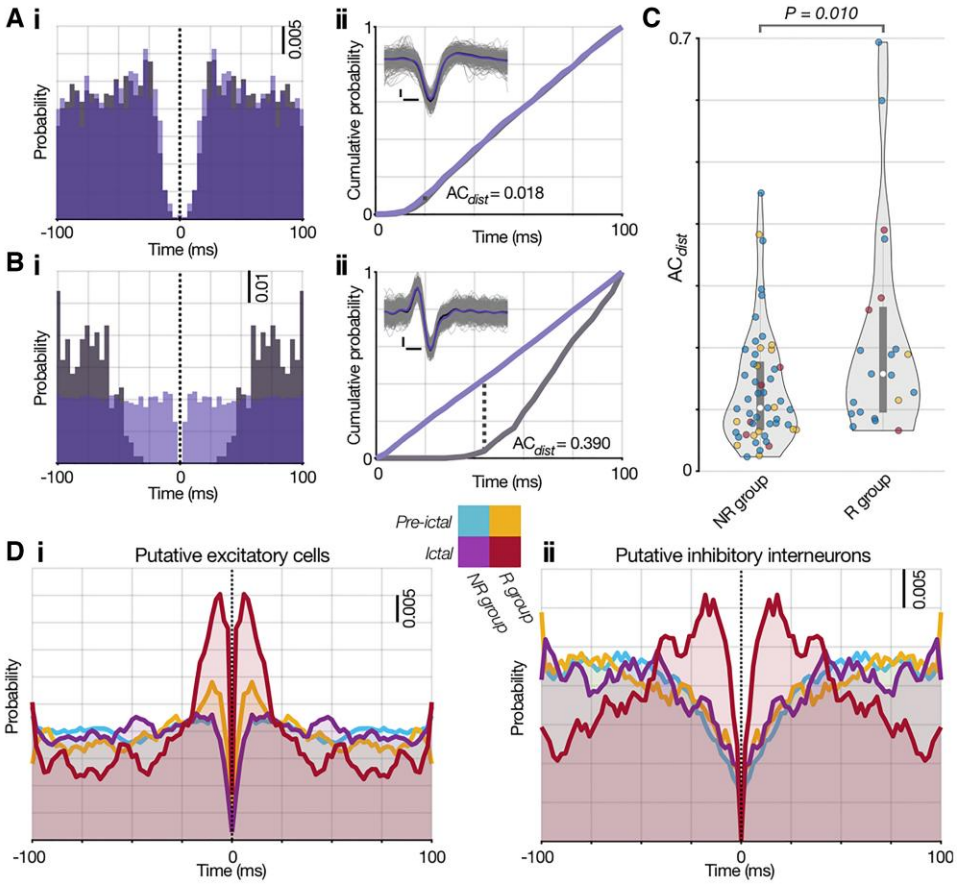

Figure 8 Alterations to cell-intrinsic firing properties in recruited tissue. (**A** and **B**) Example autocorrelograms from the pre-ictal (grey) and ictal (purple) epochs for two putative fast-spiking (FS) interneurons, with one showing stability in firing pattern [**A**(**i**)] and the other transitioning to tonic firing during the seizure [**B**(**i**)]. [**A**(**ii**) and **B**(**ii**)] Cumulative probability plots and calculated AC_{dist} values. Stability of spike shapes are shown by the superimposed plots of all waveforms (*inset*, grey) with preictal and ictal means overlaid in black and purple, respectively. Scale bars = 0.2 ms, 20 μV (**A**) and 10 μV (**B**). (**C**) Population AC_{dist} values by group and cell-type. In order to derive meaningful autocorrelation patterns over the 100 ms window, this was limited to units with firing rates ≥0.2 spikes s^{-1} (i.e. at least 20 spikes contributing to the autocorrelation) (**D**) Average autocorrelograms for each epoch and group, for putative (**i**) excitatory and (**ii**) inhibitory cells, showing the distinctive increase in burst firing (within 10 ms) for excitatory cells and shift from quintessential inhibitory interneuron firing pattern to a bursting pattern specific to the recruited group. Colours as per key: blue and yellow for the pre-ictal epoch in groups NR and R, respectively; orange and red for NR and R in the ictal epoch.

transitions towards burstiness. The recruited group showed more burstiness than the non-recruited group in both excitatory (AC_{dist}+: 0.19 ± 0.20 versus 0.09 ± 0.08; $P = 0.015$, unpaired *t*-test) and inhibitory cells (AC_{dist}+: 0.25 ± 0.13 versus 0.08 ± 0.10; $P = 0.014$, unpaired *t*-test), with inhibitory cells in the recruited group displaying a marked transition from cell-intrinsic steady-firing to burst-firing during the seizure (Fig. 8D).

Discussion

Seizure localization remains a significant challenge, limiting the efficacy of surgical management of refractory focal epilepsy. We have previously identified a critical division between neocortical regions that appear to be involved in seizures on EEG recordings: core territories that are 'recruited' into a seizure, driving its propagation, versus penumbral tissue that is secondarily impacted by the ictal discharges but is not actively driving the seizure.[1,6] However, it is not clear how this dual-territory framework might apply to mesial temporal structures given the unique role of this region in temporal lobe epilepsy. Moreover, relating these territories to clinically accessible metrics is complex, as macroelectrode signals are dominated by synaptic input to the region, rather than the local neuronal firing (the output).[65] To address these questions, we utilized human multiscale recordings from limbic structures to identify modes of neural activity during seizures, linked to electroclinical metrics of site-specific seizure involvement.

Three distinguishable seizure territories

The combined dataset of nearest macro- and micro-electrode features demonstrated three distinct ictal activity patterns in limbic structures, with one group (R) displaying an increase in synchronous multi-unit firing entrained to the ictal rhythm and extracellular action potential waveform changes consistent with paroxysmal depolarization (Fig. 3). Both features have been observed during ictal recruitment in human and animal neocortical recordings.[1,3,5] The strong alignment of group R with the clinical assessment of the EZ and greater interictal HFO rate, along with predictions from previous studies of neocortical focal epilepsy in animal models and humans, supports our conclusion that the observed neuronal activity features specific to group R are representative of local ictal

recruitment. Furthermore, several instances of simultaneous recording of neural patterns indicative of recruitment and non-recruitment (group NR) provides new support for our previously described hypothesis of dual, co-existing but physically separate seizure territories: a relatively small ictal core is surrounded by penumbra that may show the EEG signature of a seizure but in which neural firing is restrained by intact inhibition.[1,6,52,66]

While all analyses were performed blind to the clinical assessment of seizure onset, of 20 total macro-micro pairs interpreted to be located in EZ, 19 were in group R. This accuracy is rather higher than is seen in neocortex, where the clinically determined EZ overestimates the spatial extent of tissue recruitment.[1,43,52] Given the prevalence of hippocampal recordings in this group (74%), one possible explanation is the ease of detecting seizure activity with sEEG in hippocampal structures given its unique cytoarchitecture and the relatively dense hippocampal electrode coverage. An alternative explanation might be that hippocampus is highly susceptible to ictal recruitment compared to neocortex, withstanding the synaptic barrages for less time, thereby resulting in minimal time between the first EEG signatures of seizure activity and subsequent recruitment of local neurons. Such region-specific differences of ictal dynamics would be in keeping with *in vitro* observations of differing neocortical and hippocampal ictal patterns in animals[67] and in varying seizure susceptibility and ictal patterns in resected human tissue.[68]

We also detected a subcluster within the non-recruited group (NR_1), in which macroelectrode-derived metrics did not reveal ictal recruitment, but microelectrode-derived single and multi-unit metrics more closely resembled the pattern seen in the recruited group, suggesting feedforward effects from the seizure at these sites. This is consistent both with the neuronal activity expected in penumbral territories receiving synaptic barrages from the seizure core[1,5,69] and with our recently published observations of neocortical ictal recruitment operating at the level of single neurons.[3] Such sites may represent a strongly connected node involved in the propagation of the seizure itself[70,71] by amplifying the excitatory barrages experienced at the distant site and increasing the possibility of secondary recruitment at that site. Another possibility is that incipient recruitment could result from locally impaired inhibition. A rodent model of acute neocortical seizures has demonstrated that focal seizures could generate distant secondary foci in the absence of pathologically reinforced structural alterations as a result of local inhibitory breakdown, which can appear as coordinated network activity.[8] In either scenario, subgroup NR_1 may be framed as representing secondary regions that have the potential to transition into an ictal state, while NR_2 is dominated by territories less impacted by the ongoing seizure.

An intriguing question is whether NR_1 sites have increased potential to become dominant seizure foci following resection/disconnection of the primary focus. Consider the post-surgical outcomes of Patients 1 and 13, who both had extratemporal SOZs with hippocampal recordings belonging to subgroup NR_1: Patient 13 had an Engel 3A outcome at 16.5 months following an insular resection, and Patient 1 had a frontal lobe resection with an Engel 1A outcome at 19 months. However, Patient 1 went on to have a second surgical evaluation in light of non-specific sensory auras that later arose, although with no evidence of hippocampal involvement (Supplementary Table 1). Future studies may elucidate if sites with NR_1 activity patterns might predict post-surgical failure.

Of the examined neuronal activity patterns, high-gamma entrainment to the ictal rhythm, as indexed by PLV_{HG} obtained from the nearest macroelectrode, was the only metric capable of distinguishing the two ictal territories at the level of an individual seizure and recording site. This finding is consistent with previous studies validating EEG-derived metrics that simultaneously assess both high- and low-frequency information, including the related phase-locked high-gamma metric[43,52] and the epileptogenicity index, which incorporates line-length but does not consider phase-locking.[72] Even with implanted depth electrodes, the ictal wavefront (a band of tonic firing at the leading edge of an advancing seizure), is unfortunately largely invisible to clinical EEG recordings likely due to abolishing the periodic firing that is a basic requirement for generating oscillatory EEG features.[1,6,35,40,43] High-gamma activity phase-locked to the underlying ictal rhythm, however, has been shown to increase sharply following passage of the ictal wavefront but not at sites that did not demonstrate an ictal wavefront.[1,43] PLV_{HG}, therefore, is a practical method of identifying ictal recruitment on a per seizure basis. Conversely, measures such as multi-unit firing rate or high-gamma activity, while demonstrating measurable differences between groups, may not reliably categorize the recruitment status of an individual channel's recording.

Heterogenous single-unit changes during seizures

While the anticipated difference in multi-unit firing between recruited and non-recruited groups was found, the high degree of heterogeneity of firing within both groups differed sharply from our prior neocortical findings.[1,3,5,35,43] Although heterogeneity in ictal firing has previously been reported in human recordings,[17,18,20] we had hypothesized that heterogeneous firing would be much less prominent in recruited brain areas, on the basis of our prior observations in neocortical microelectrode human recordings.[1,3] We explored single-unit firing in detail using our recently developed template-matching method, which was designed to avoid confounding firing rate assessment due to changes in noise level and action potential waveform shape.[3,4]

Although a natural decrease in firing rate due to the well-known hyperpolarization that follows epileptiform discharges may occur, average firing rates remained high in our prior analyses of neocortical recordings.[1,3,4,35] In contrast, across all 156 single units in this study, we found that a high proportion (69%) of all cell-types demonstrated decreases in ictal firing rates (Fig. 6A and B), with some ceasing firing altogether. This prominent decrease appears to contradict the simultaneous findings of increased high-gamma amplitude and PLV_{HG}, recorded from the nearby macroelectrode, due to the association of electrocorticography (ECoG)-recorded high-gamma activity with intense multi-unit firing.[35,36] One possible explanation is that single-unit detection is inherently biased towards high firing rate neurons, and these may be more likely to decrease their firing rate than neurons that fire less frequently.

Firing patterns of fast-spiking interneurons

Recent work has uncovered evidence of marked FS interneuron firing rate increases at seizure onset, with a proposed 'excitatory rebound' mechanism contributing to ictogenesis.[28,73] A subsequent study of human microelectrode data reported finding evidence of increased interneuron firing early in the seizure in a group of nine patients with low-voltage fast onset patterns.[30] In our dataset, one of 17 FS interneurons, an interneuron from the recruited group, demonstrated a striking activity pattern of transient increases in firing followed by cessation of firing (Fig. 7A). This FS interneuron firing pattern has been ascribed to a rapidly increasing excitatory drive which may result in simultaneous weakening or even reversal

of the GABA current in the postsynaptic cell due to intracellular chloride loading.[4,74-78] Under this scenario, increases in pyramidal cell firing are expected following the sharp increase in FS interneuron activity, as we have demonstrated in neocortical human recordings.[4] This increase was not observed in our data in any group (Supplementary Fig. 6), though it should be noted that in this particular example of interneuronal activity, there were no pyramidal cells captured at the same electrode. Nonetheless, the interneuronal activity seen here is consistent with observations in a pilocarpine-mouse model where interneuronal inactivation during the seizure was common, while pre-ictal activation or inactivation was heterogeneous and dependent on hippocampal subfield.[27]

FS interneuron depolarization block is another mechanism that has been proposed to underlie the interictal-ictal transition and subsequent recruitment of post-synaptic pyramidal cells.[25,76,79,80] Yet, we did not find definitive evidence of depolarization block in the sampled mesial structures to explain either the cessation or reduction in FS interneuron firing, despite the clear presence of a highly excitatory state: single-unit trajectories in these recordings were generally stable and clear of the detection threshold during the seizure (meaning that drop-out was not explained by small fluctuations in the shape of the unit; Fig. 6E), and the majority of FS interneuron firing rate reductions occurred without a prior increase (Fig. 7B and C).

For the limbic seizures in this study, these findings suggest that the posited weakening of local inhibition, while occurring sporadically, is unlikely to be a major driver of hippocampal seizures. Nevertheless, there is some evidence for feedforward inhibition and its subsequent ictal impairment. The largest transient increases in FS interneuron firing, as well as maximal waveshape changes of the FS population prior to reduction in firing, occurred in the group that remained unrecruited, though had multi-unit evidence of oncoming ictal activity (NR_1; Supplementary Figs 5 and 6), and once recruited, interneurons showed perturbed, bursting firing patterns (Fig. 8). As such, inhibition is likely compromised to a degree, but may not be the complete inhibitory failure that has been documented in slice studies or neocortical recordings.

We note that, as is common in the patient population undergoing invasive monitoring of mesial temporal structures,[81] none of the patients in this study had mesial temporal sclerosis on preoperative imaging or tissue pathology (Supplementary Table 1). It may be that the non-sclerotic hippocampus, while readily becoming excitable, is less susceptible to complete inhibitory collapse compared to neocortex as a result of its unique cytoarchitectural structure. We propose that the predominance of single-unit firing rate reductions provides evidence for at least moderately maintained inhibition in the hippocampus for the majority of recordings in the recruited group, i.e. that if inhibitory failure does occur in the hippocampus during seizures, it is not a common phenomenon in this study population. This suggests a possible alternative scenario in which the hippocampus, while clearly in a high excitability, rhythmic activity state, may not have been completely recruited, instead amplifying seizure activity driven from a nearby source but not itself primarily driving seizure activity. Similar decreases in hippocampal interneuron firing were reported in seven patients with known neocortical onsets and suspected mesial temporal spread.[33] This raises the interesting question of whether complete versus partial hippocampal recruitment may have a bearing on whether hippocampal removal can successfully prevent seizures, and whether clinically accessible information can be used to differentiate these two activity states. The relatively low seizure freedom rates following selective thermal ablation of hippocampus and other mesial temporal structures[81,82] suggest that better patient selection and seizure freedom rates are possible if we can reliably distinguish the hippocampus in a seizure amplifier versus seizure driver state.

Data availability

The data that support the findings of this study are available upon reasonable request from the corresponding author. The data are not publicly available to protect the privacy of research participants.

Funding

The authors acknowledge funding from NIH: R01 NS084142, R01 NS110669, and R01 NS095368 (C.A.S.).

Competing interests

G.M.M. is an investigator and on the publication committee for the 'Stereotactic Laser Ablation in Temporal Epilepsy' (SLATE) trial funded by Medtronic, plc. None of the patients in this study were enrolled in the SLATE trial. The other authors report no competing interests.

Supplementary material

Supplementary material is available at *Brain* online.

References

1. Schevon CA, Weiss SA, McKhann G, *et al*. Evidence of an inhibitory restraint of seizure activity in humans. *Nat Commun*. 2012;3:1060-1011.
2. Eissa TL, Dijkstra K, Brune C, *et al*. Cross-scale effects of neural interactions during human neocortical seizure activity. *PNAS*. 2017;114:10761-10766.
3. Merricks EM, Smith EH, Emerson RG, *et al*. Neuronal firing and waveform alterations through ictal recruitment in humans. *J Neurosci*. 2021;41:766-779.
4. Tryba AK, Merricks EM, Lee S, *et al*. Role of paroxysmal depolarization in focal seizure activity. *J Neurophysiol*. 2019;122:1861-1873.
5. Merricks EM, Smith EH, McKhann GM, *et al*. Single unit action potentials in humans and the effect of seizure activity. *Brain*. 2015;138(10):2891-2906.
6. Trevelyan AJ, Sussillo D, Watson BO, Yuste R. Modular propagation of epileptiform activity: Evidence for an inhibitory veto in neocortex. *J Neurosci*. 2006;26:12447-12455.
7. Trevelyan AJ, Sussillo D, Yuste R. Feedforward inhibition contributes to the control of epileptiform propagation speed. *J Neurosci*. 2007;27:3383-3387.
8. Liou J, Ma H, Wenzel M, *et al*. Role of inhibitory control in modulating focal seizure spread. *Brain*. 2018;141:2083-2097.
9. Goldensohn ES, Purpura DP. Intracellular potentials of cortical neurons during focal epileptogenic discharges. *Science*. 1963;139:840-842.
10. Dichter MA, Ayala GF. Cellular mechanisms of epilepsy: A status report. *Science*. 1987;237:157-164.
11. Matsumoto H, Ajmone Marsan C. Cortical cellular phenomena in experimental epilepsy: Ictal manifestations. *Exp Neurol*. 1964;9:305-326.

12. Spencer SS. Neural networks in human epilepsy: Evidence of and implications for treatment. *Epilepsia*. 2002;43:219-227.
13. Kramer MA, Cash SS. Epilepsy as a disorder of cortical network organization. *Neuroscientist*. 2012;18:360-372.
14. Jirsa VK, Proix T, Perdikis D, *et al*. The virtual epileptic patient: Individualized whole-brain models of epilepsy spread. *NeuroImage*. 2017;145:377-388.
15. Babb TL, Crandall PH. Epileptogenesis of human limbic neurons in psychomotor epileptics. *Electroencephalogr Clin Neurophysiol*. 1976;40:225-243.
16. Wyler AR, Ojemann GA, Ward AA. Neurons in human epileptic cortex: Correlation between unit and EEG activity. *Ann Neurol*. 1982;11:301-308.
17. Truccolo W, Donoghue JA, Hochberg LR, *et al*. Single-neuron dynamics in human focal epilepsy. *Nat Neurosci*. 2011;14:635-641.
18. Bower MR, Buckmaster PS. Changes in granule cell firing rates precede locally recorded spontaneous seizures by minutes in an animal model of temporal lobe epilepsy. *J Neurophysiol*. 2008;99:2431-2442.
19. Bower MR, Stead M, Meyer FB, *et al*. Spatiotemporal neuronal correlates of seizure generation in focal epilepsy. *Epilepsia*. 2012;53:807-816.
20. Lambrecq V, Lehongre K, Adam C, *et al*. Single-unit activities during the transition to seizures in deep mesial structures. *Ann Neurol*. 2017;82:1022-1028.
21. Tobochnik S, Tai P, McKhann GM, Schevon CA. Seizure activity across scales from neuronal population firing to clonic motor semiology. *J Clin Neurophysiol*. 2020;37:462-464.
22. Babb TL, Wilson CL, Isokawa-Akesson M. Firing patterns of human limbic neurons during stereoencephalography (SEEG) and clinical temporal lobe seizures. *Electroencephalogr Clin Neurophysiol*. 1987;66:467-482.
23. Babb TL, Carr E, Crandall PH. Analysis of extracellular firing patterns of deep temporal lobe structures in man. *Electroencephalogr Clin Neurophysiol*. 1973;34:247-257.
24. Miri ML, Vinck M, Pant R, Cardin JA. Altered hippocampal interneuron activity precedes ictal onset. *eLife*. 2018;7:1277.
25. Ziburkus J, Cressman JR, Barreto E, Schiff SJ. Interneuron and pyramidal cell interplay during in vitro seizure-like events. *J Neurophysiol*. 2006;95:3948-3954.
26. Grasse DW, Karunakaran S, Moxon KA. Neuronal synchrony and the transition to spontaneous seizures. *Exp Neurol*. 2013;248(C):72-84.
27. Toyoda I, Fujita S, Thamattoor AK, Buckmaster PS. Unit activity of hippocampal interneurons before spontaneous seizures in an animal model of temporal lobe epilepsy. *J Neurosci*. 2015;35:6600-6618.
28. de Curtis M, Avoli M. GABAergic networks jump-start focal seizures. *Epilepsia*. 2016;57:679-687.
29. Gnatkovsky V, Librizzi L, Trombin F, de Curtis M. Fast activity at seizure onset is mediated by inhibitory circuits in the entorhinal cortex in vitro. *Ann Neurol*. 2008;64:674-686.
30. Elahian B, Lado NE, Mankin E, *et al*. Low-voltage fast seizures in humans begin with increased interneuron firing. *Ann Neurol*. 2018;84:588-600.
31. Chang M, Dian JA, Dufour S, *et al*. Brief activation of GABAergic interneurons initiates the transition to ictal events through post-inhibitory rebound excitation. *Neurobiol Dis*. 2018;109(A):102-116.
32. Shiri Z, Manseau F, Lévesque M, *et al*. Interneuron activity leads to initiation of low-voltage fast-onset seizures: Epileptiform synchronization. *Ann Neurol*. 2015;77:541-546.
33. Misra A, Long X, Sperling MR, *et al*. Increased neuronal synchrony prepares mesial temporal networks for seizures of neocortical origin. *Epilepsia*. 2018;3(Suppl 2):219-214.
34. Groppe DM, Bickel S, Dykstra AR, *et al*. iELVis: An open source MATLAB toolbox for localizing and visualizing human intracranial electrode data. *J Neurosci Methods*. 2017;281:40-48.
35. Smith EH, Liou J, Davis TS, *et al*. The ictal wavefront is the spatiotemporal source of discharges during spontaneous human seizures. *Nat Commun*. 2016;7:11098.
36. Ray S, Maunsell JHR. Different origins of gamma rhythm and high-gamma activity in macaque visual cortex. *PLoS Biol*. 2011;9:e1000610.
37. Eissa TL, Tryba AK, Marcuccilli CJ, *et al*. Multiscale aspects of generation of high-gamma activity during seizures in human neocortex. *eNeuro*. 2016;3:ENEURO.0141-15.2016-17.
38. Navarrete M, Alvarado-Rojas C, Le Van Quyen M, Valderrama M. RIPPLELAB: A comprehensive application for the detection, analysis and classification of high frequency oscillations in electroencephalographic signals. *PLoS One*. 2016;11:e0158276.
39. Zijlmans M, Worrell GA, Dümpelmann M, *et al*. How to record high-frequency oscillations in epilepsy: A practical guideline. *Epilepsia*. 2017;58:1305-1315.
40. Liou J, Smith EH, Bateman LM, *et al*. A model for focal seizure onset, propagation, evolution, and progression. *eLife*. 2020;9:e50927.
41. Kramer MA, Truccolo W, Eden UT, *et al*. Human seizures self-terminate across spatial scales via a critical transition. *Proc Natl Acad Sci U S A*. 2012;109:21116-21121.
42. Penfield W, Jasper H. *Epilepsy and the functional anatomy of the human brain*. Little, Brown & Co.; 1954.
43. Weiss SA, Banks GP, McKhann GM, *et al*. Ictal high frequency oscillations distinguish two types of seizure territories in humans. *Brain*. 2013;136(Pt 12):3796-3808.
44. Vanhatalo S, Palva JM, Holmes MD, *et al*. Infraslow oscillations modulate excitability and interictal epileptic activity in the human cortex during sleep. *PNAS*. 2004;101:5053-5057.
45. Penny WD, Duzel E, Miller KJ, Ojemann JG. Testing for nested oscillation. *J Neurosci Methods*. 2008;174:50-61.
46. Box GEP, Cox DR. An analysis of transformations. *J R Stat Soc Series B (Methodol)*. 1964;26:211-252.
47. Hennig C. Cluster-wise assessment of cluster stability. *Comput Stat Data Anal*. 2007;52:258-271.
48. Hennig C. fpc: Flexible procedures for clustering. Accessed 8 January 2022. https://cran.r-project.org/web/packages/fpc/fpc.pdf
49. R Core Team. *R: A language and environment for statistical computing*. R Foundation for Statistical Computing; 2022. https://www.R-project.org/
50. Goodpaster AM, Kennedy MA. Quantification and statistical significance analysis of group separation in NMR-based metabonomics studies. *Chemometr Intell Lab Syst*. 2011;109:162-170.
51. Esteller R, Echauz J, Tcheng T, *et al*. Line length: an efficient feature for seizure onset detection. In: *2001 Conference Proceedings of the 23rd Annual International Conference of the IEEE Engineering in Medicine and Biology Society*. IEEE. vol. 2. 2001:1707-1710.
52. Weiss SA, Lemesiou A, Connors R, *et al*. Seizure localization using ictal phase-locked high gamma: A retrospective surgical outcome study. *Neurology*. 2015;84:2320-2328.
53. Ardid S, Vinck M, Kaping D, *et al*. Mapping of functionally characterized cell classes onto canonical circuit operations in primate prefrontal cortex. *J Neurosci*. 2015;35:2975-2991.
54. Mountcastle VB, Talbot WH, Sakata H, Hyvärinen J. Cortical neuronal mechanisms in flutter-vibration studied in unanesthetized monkeys. Neuronal periodicity and frequency discrimination. *J Neurophysiol*. 1969;32:452-484.
55. Erisir A, Lau D, Rudy B, Leonard CS. Function of specific K(+) channels in sustained high-frequency firing of fast-spiking neocortical interneurons. *J Neurophysiol*. 1999;82:2476-2489.
56. Rudy B, Fishell G, Lee S, Hjerling Leffler J. Three groups of interneurons account for nearly 100% of neocortical GABAergic neurons. *Dev Neurobiol*. 2011;71:45-61.
57. Petersen PC, Siegle JH, Steinmetz NA, *et al*. Cellexplorer: A framework for visualizing and characterizing single neurons. *Neuron*. 2021;109:3594-3608.e2.

58. Barthó P, Hirase H, Monconduit L, *et al*. Characterization of neocortical principal cells and interneurons by network interactions and extracellular features. *J Neurophysiol*. 2004;92:600-608.
59. Hill DN, Mehta SB, Kleinfeld D. Quality metrics to accompany spike sorting of extracellular signals. *J Neurosci*. 2011;31:8699-8705.
60. Schubert E, Gertz M. Intrinsic t-stochastic neighbor embedding for visualization and outlier detection. In: Beecks C, Borutta F, Kröger P, Seidl T, eds. *Similarity search and applications*. Springer International Publishing; 2017:188-203.
61. Duda RO, Hart PE, Stork DG. *Pattern classification*. John Wiley & Sons, Inc.; 2000.
62. Caliński T, Harabasz J. A dendrite method for cluster analysis. *Commun Stat*. 1974;3:1-27.
63. Jacobs J, Staba R, Asano E, *et al*. High-frequency oscillations (HFOs) in clinical epilepsy. *Prog Neurobiol*. 2012;98:302-315.
64. Cimbalnik J, Kucewicz MT, Worrell G. Interictal high-frequency oscillations in focal human epilepsy. *Curr Opin Neurol*. 2016;29:175-181.
65. Buzsàki G, Anastassiou CA, Koch C. The origin of extracellular fields and currents—EEG, ECoG, LFP and spikes. *Nat Rev Neurosci*. 2012;13:407-420.
66. Schevon CA, Tobochnik S, Eissa T, *et al*. Multiscale recordings reveal the dynamic spatial structure of human seizures. *Neurobiol Dis*. 2019;127:303-311.
67. Codadu NK, Parrish RR, Trevelyan AJ. Region-specific differences and areal interactions underlying transitions in epileptiform activity. *J Physiol*. 2019;597:2079-2096.
68. Reyes-Garcia SZ, Scorza CA, Araújo NS, *et al*. Different patterns of epileptiform-like activity are generated in the sclerotic hippocampus from patients with drug-resistant temporal lobe epilepsy. *Sci Rep*. 2018;8:7116.
69. Smith EH, Merricks EM, Liou J-Y, *et al*. Dual mechanisms of ictal high frequency oscillations in human rhythmic onset seizures. *Sci Rep*. 2020;10:19166.
70. Blumenfeld H. What is a seizure network? Long-range network consequences of focal seizures. *Adv Exp Med Biol*. 2014;813:63-70.
71. Fujita S, Toyoda I, Thamattoor AK, Buckmaster PS. Preictal activity of subicular, CA1, and dentate gyrus principal neurons in the dorsal hippocampus before spontaneous seizures in a rat model of temporal lobe epilepsy. *J Neurosci*. 2014;34:16671-16687.
72. Bartolomei F, Chauvel P, Wendling F. Epileptogenicity of brain structures in human temporal lobe epilepsy: A quantified study from intracerebral EEG. *Brain*. 2008;131:1818-1830.
73. Paz JT, Huguenard JR. Microcircuits and their interactions in epilepsy: Is the focus out of focus? *Nat Neurosci*. 2015;18:351-359.
74. Pallud J, Le Van Quyen M, Bielle F, *et al*. Cortical GABAergic excitation contributes to epileptic activities around human glioma. *Sci Transl Med*. 2014;6:244ra89.
75. Lillis KP, Kramer MA, Mertz J, *et al*. Pyramidal cells accumulate chloride at seizure onset. *Neurobiol Dis*. 2012;47:358-366.
76. Cammarota M, Losi G, Chiavegato A, *et al*. Fast spiking interneuron control of seizure propagation in a cortical slice model of focal epilepsy. *J Physiol*. 2013;591(4):807-822.
77. Alfonsa H, Merricks EM, Codadu NK, *et al*. The contribution of raised intraneuronal chloride to epileptic network activity. *J Neurosci*. 2015;35:7715-7726.
78. Ellender TJ, Raimondo JV, Irkle A, *et al*. Excitatory effects of parvalbumin-expressing interneurons maintain hippocampal epileptiform activity via synchronous afterdischarges. *J Neurosci*. 2014;34:15208-15222.
79. Yi F, DeCan E, Stoll K, *et al*. Muscarinic excitation of parvalbumin-positive interneurons contributes to the severity of pilocarpine-induced seizures. *Epilepsia*. 2015;56:297-309.
80. Călin A, Ilie AS, Akerman CJ. Disrupting epileptiform activity by preventing parvalbumin interneuron depolarization block. *J Neurosci*. 2021;41:9452-9465.
81. Michalak AJ, Greenblatt A, Wu S, *et al*. Seizure onset patterns predict outcome after stereo-electroencephalography-guided laser amygdalohippocampotomy. *Epilepsia*. 2023;64:1568-1581.
82. Youngerman BE, Banu MA, Khan F, *et al*. Long-term outcomes of mesial temporal laser interstitial thermal therapy for drug-resistant epilepsy and subsequent surgery for seizure recurrence: A multi-centre cohort study. *J Neurol Neurosurg Psychiatry*. Published online 25 June 2023. doi:10.1136/jnnp-2022-330979
83. Van der Maaten L, Hinton G. Visualizing data using t-SNE. *J Mach Learn Res*. 2008;9:2579-2605.
84. Vajda I, van Pelt J, Wolters P, *et al*. Low-frequency stimulation induces stable transitions in stereotypical activity in cortical networks. *Biophys J*. 2008;94:5028-5039.